

This is the accepted manuscript made available via CHORUS. The article has been published as:

Complex nanoprecipitate structures induced by irradiation in immiscible alloy systems

Shipeng Shu, P. Bellon, and R. S. Averback

Phys. Rev. B **87**, 144102 — Published 8 April 2013

DOI: [10.1103/PhysRevB.87.144102](https://doi.org/10.1103/PhysRevB.87.144102)

Novel nanoprecipitate structures induced by irradiation in immiscible alloy systems

Shipeng Shu, P. Bellon, and R. S. Averback

Department of Materials Science and Engineering,

University of Illinois at Urbana-Champaign, Urbana, Illinois 61801, USA

(Dated: March 20, 2013)

We investigate the fundamentals of compositional patterning induced by energetic particle irradiation in model A-B substitutional binary alloys using kinetic Monte Carlo simulations. The study focuses on a novel type of nanostructure that was recently observed in dilute Cu-Fe and Cu-V alloys, where precipitates form within precipitates, a morphology that we term “cherry-pit” structures. The simulations show that the domain of stability of these cherry-pit structures depends on the thermodynamic and kinetic asymmetry between the A and B elements. In particular, both lower solubilities and diffusivities of A in B compared to those of B in A, favor the stabilization of these cherry-pit structures for A-rich average compositions. The simulation results are rationalized by extending the analytic model introduced by Frost and Russell for irradiation-induced compositional patterning so as to include the possible formation of pits within precipitates. The simulations indicate also that the pits are dynamical structures that undergo nearly periodic cycles of nucleation, growth, and absorption by the matrix.

I. INTRODUCTION

Dissipative material systems are known to develop non-equilibrium phases and patterns in a wide variety of situations, e.g., in chemical reactions, macromolecular assemblies, cell membranes, ecosystems, lasing systems, weather, and earthquakes¹. These findings have particular importance for materials that are subjected to energetic particle irradiation, for example in nuclear reactors.² The primary concern is that non-equilibrium phases and microstructures often impact negatively the performance of these materials during their service life. Irradiation, however, can also be used to stabilize novel microstructures through self-organization reactions, with the potential of improving materials properties. The present work focuses on the fundamental processes responsible for self-organization under irradiation and reports on a novel structure, where matrix atom precipitates form within solute-rich precipitates in dilute binary alloys.

The stabilization of nano-structures by irradiation was first reported by Nelson and co-workers³ for Ni-Al alloys. These authors showed that after ion irradiation at intermediate temperature ($T = 550^\circ\text{C}$) the alloy had reached a steady state microstructure comprised of nanometer-size ordered precipitates in a Ni-rich matrix. The origin of this mesoscale organization was attributed to the fact that the mixing forced by energetic ions takes place over distances far exceeding the typical length scale for thermally activated atomic jumps, which is typically one nearest neighbor distance in the host lattice, a_{nn} . Compositional patterning induced by irradiation has since been reported in several immiscible binary Cu alloys,^{4,5} and in systems comprised of metallic precipitates in silica^{6,7}. In particular, Krasnochtchikov et al.⁴ used magnetic measurements to carry out a systematic investigation of the evolution of Co precipitates in dilute Cu-Co alloys subjected to Kr irradiations using various irradiation temperature, doses, and initial microstructures.

They confirmed that the stabilization by irradiation of finite size precipitates only occurs within a specific range of irradiation temperatures. At too low of temperature the alloys homogenize and at too high of temperature, precipitates coarsen. Chee et al.⁵ reported similar results for other dilute Cu-base alloys, including Cu-Ag, investigated by X-ray diffraction (XRD) and transmission electron microscopy (TEM) and Cu-Fe, characterized by atom probe tomography (APT). The atomic reconstruction maps in Cu-Fe showed, quite surprisingly, that the Fe-rich precipitates contained a significant amount of Cu and that these Cu atoms would often form precipitates within the Fe-rich precipitates,⁸ as illustrated in Fig. 1. These unusual precipitate structures are akin to core shell structures found in ternary alloys after thermal annealing,^{9–11} but here the core consists host matrix atoms. We refer to these structures as “cherry-pit” nanostructures. We note that morphologically similar nanostructures, known as double emulsions, have also been reported in immiscible liquids.¹² While compositional patterning induced by irradiation is reasonably well understood from a fundamental perspective, as we will detail in the next paragraph, the stabilization of cherry-pit nano-structures by irradiation has not been discussed previously. The main objective of the present work, therefore, is to elucidate how these cherry-pit nano-structures develop, and to identify the irradiation conditions required for their stabilization.

The stabilization of cherry-pit structures during irradiation is closely related to compositional patterning, therefore we briefly review some key results previously obtained by modeling and atomistic simulations. As indicated above, Nelson et al.³ recognized that an essential physical parameter for patterning was the long range recoil of atoms. Frost and Russell^{13,14} later proposed a model for the evolution of precipitates in a binary immiscible alloy where irradiation forces the relocation of atoms to a distance $R \gg a_{nn}$, and they found that, when this finite-range forced mixing competes with



FIG. 1. Microstructure found by atom probe reconstruction of a $\text{Cu}_{88}\text{Fe}_{12}$ sample, irradiated by 1.8 MeV Kr^+ ions at 350°C to a dose of 3×10^{16} ions/ cm^2 . The cross section of the 1-nm thick layer of atoms is about 50 nm in diameter. The Fe atoms (yellow) have been minimized to make the Cu atoms (red) inside the Fe precipitate more visible. Adapted from ref. 8.

thermodynamically driven phase separation, finite size precipitates could be stabilized. An important simplification introduced in this model, however, is that the ballistic jumps transfer solute atoms from precipitates to the matrix, but not from the matrix to the precipitates. This simplification can sometimes lead to unphysical results,¹⁵ particularly for electron and light ion irradiations for which the average recoil distances are comparable to a_{nn} , and recoil-induced back diffusion should be important. Indeed, according to the Frost-Russell model, even for low values of R , compositional patterning is always predicted in some region of the irradiation parameter space, whereas compositional patterning induced by electron or light ion irradiations has never been reported experimentally.^{2,16}

Enrique and Bellon later introduced a kinetic model that accounts for the full contribution of ballistic jumps.¹⁷ This model predicts that the competition between finite range ballistic mixing and thermal decomposition can stabilize three different steady states, namely a homogeneous single-phase state, a phase-separated state where phases co-exist at a macroscopic scale, and a phase-separated state where phases co-exist at a finite length scale, also referred to as compositional patterning (see Fig. 2). For a given average composition, the domains of existence of these three distinct steady states were calculated as a function of the mixing distance R and the reduced forcing parameter $\gamma = \Gamma/M$, where Γ is the ballistic jump frequency, and M is the thermal mobility, possibly enhanced by radiation. Note in particular that compositional patterning is only found when the relocation distance R exceeds some critical value R_c . The above three steady states and their corresponding transitions were confirmed by kinetic Monte Carlo (KMC) simulations on a rigid face centered cubic (fcc) lattice.^{17–19} One important feature of the patterning regime for what

follows is that the steady state size of the precipitates increases continuously with decreasing γ , until undergoing a first-order transition to macroscopic phase separation.

In the present work, we employ similar KMC simulations to investigate more broadly the stabilization of nanostructures by irradiation in a generic $A_{1-c}B_c$ alloy on an fcc lattice. In particular we vary systematically the composition of the alloy, from the dilute compositions investigated by Krasnochtchekov⁴ to the equiatomic composition investigated by Enrique et al.¹⁹ We also consider the effect of the asymmetries in thermodynamic interactions and diffusion coefficients in the A - B alloys. Indeed, while past simulations on compositional patterning induced by ballistic mixing only considered $A_{1-c}B_c$ binary alloy systems that are invariant under the transformation $c \leftrightarrow (1 - c)$, it is well documented that thermodynamic and kinetic asymmetries can significantly affect kinetic pathways during thermal annealing,^{20–23} as well as under irradiation.²³ Furthermore these asymmetries are always present in real alloy systems, and it is thus important to evaluate their effect on self-organization. By varying composition and asymmetries, we find that there exists in fact five distinct steady states for alloys under irradiation: the three noted above, plus two associated with cherry-pit structures. We show that these five regimes can be rationalized by extending the Frost-Russell model^{13,14} and combining it with the dynamical phase diagram predicted by the Enrique-Bellon model.¹⁷ Lastly we show that our simulations provide the basis for understanding the new experimental results on cherry-pit structures in irradiated Cu-Fe and Cu-V alloys.

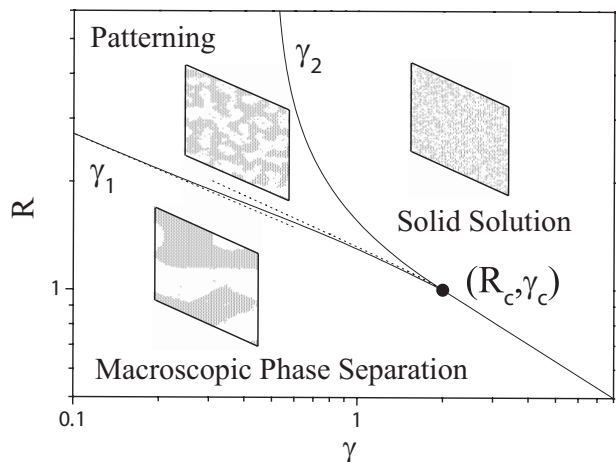


FIG. 2. Dynamical phase diagram for an irradiated $A_{50}B_{50}$ alloy. Steady-state regimes are illustrated as a function of mixing distance R (normalized by the equilibrium interfacial thickness) and reduced forcing parameter γ . Adapted from ref. 17.

II. KMC SIMULATIONS

The KMC simulations are based on the model described by Enrique and Bellon.¹⁸ In this model, atoms migrate by two distinct mechanisms: thermally activated jumps assisted by nearest neighbor atom-vacancy exchanges, and athermal ballistic relocations arising from atomic collisions. An immiscible binary A - B alloy is created on a rigid fcc lattice using periodic boundary conditions. A single vacancy is introduced into the system for the thermally activated atom jumps. Nearest-neighbor atomic pair interactions ($\epsilon_{AA}, \epsilon_{AB}, \epsilon_{BB}$) and atom-vacancy interactions ($\epsilon_{AV}, \epsilon_{BV}$) are used to model cohesion and vacancy formation energies of the system. Pure A and B cohesive energies are defined as $E_{coh}^A = \frac{Z}{2}\epsilon_{AA}$ and $E_{coh}^B = \frac{Z}{2}\epsilon_{BB}$; Z is the nearest neighbor site coordination number ($Z = 12$ here). The ordering energy is defined as $\omega_{AB} = 2\epsilon_{AB} - \epsilon_{AA} - \epsilon_{BB}$. Therefore a positive value of ω corresponds to an alloy system that is immiscible and phase separates at low enough temperature. Effective vacancy-atom interactions ϵ_{XV} , $X = A, B$ are used to adjust the vacancy formation energy,²⁴ which is defined by $E_{for}^{XV} = Z\epsilon_{XV} - \frac{Z}{2}\epsilon_{XX}$.

In addition, we have extended this model in order to explore the effect of asymmetric thermodynamic interactions by including triplet atomic interactions are introduced. An interaction energy is assigned to the equilateral triangles formed by three common nearest neighbor atoms. Direct counting of bonds and triplets shows that, in mean-field point approximation (Bragg-Williams), the mixing enthalpy of a homogeneous system ΔE_{mix} with triplet atomic interactions takes the form

$$\begin{aligned} \frac{\Delta E_{mix}}{N} = & \frac{Z}{2}c_Ac_B[2\epsilon_{AB} - \epsilon_{AA} - \epsilon_{BB}] \\ & + \frac{Z_t}{6}c_Ac_B[3(-\epsilon_{AAA} - \epsilon_{BBB} + \epsilon_{AAB} + \epsilon_{ABB}) \\ & + (c_A - c_B)(-\epsilon_{AAA} + \epsilon_{BBB} + 3\epsilon_{AAB} - 3\epsilon_{ABB})] \end{aligned} \quad (1)$$

where N is the total number of atoms in the system, $Z_t = 24$ is the number of first nearest neighbor triangles sharing one summit. We note that the functional dependence of the mixing enthalpy with composition is identical to the Redlich-Kister expansion used in sub-regular solution models.²⁵ For simplicity, we set the triplet atomic interactions ϵ_{AAA} and ϵ_{BBB} to be zero, so that the cohesive energies of pure A and B systems remain identical to the ones calculated with pairwise interactions. Moreover, we assume that $\epsilon_{AAB} = -\epsilon_{ABB}$, so that when $c_A = c_B$, we recover the same mixing enthalpy as in the case with pairwise interactions. When $c_A \neq c_B$, however, the mixing enthalpy deviates from the value obtained with pairwise interactions. An important consequence is that, with non-zero ϵ_{AAB} and ϵ_{ABB} , the equilibrium phase diagram is no longer invariant under the transformation $c_A \leftrightarrow c_B$, and thus the solubilities of A and B atoms are no longer equal. The frequency of thermal jumps is determined using standard-rate theory, with the activation energy calculated using a broken-

bond model,

$$\Delta E_{VX} = E_X^{SP} - \sum_m \epsilon_{mX} - \sum_n \epsilon_{nV} - \sum_{p,q} \epsilon_{pqX} \quad (2)$$

where E_X^{SP} is the saddle point energy, m and n label the nearest neighbor sites of V and X , respectively, and p, q , and X are the sites forming first nearest neighbor triangles.

As in previous works, irradiation induced mixing is simulated by randomly picking one atom and switching it with another atom according to a predetermined distribution of relocation distances. Here this distribution is chosen to be a decay exponential, $\exp(-r_{ij}/R)$, where r_{ij} is the pair separation distance, and R is the characteristic relocation distance. If not specifically noted, $R = 1.08a_{nn}$ is used in the simulations, following molecular dynamics simulation results of energetic cascades in Cu-Ag alloy irradiated with 1 MeV Kr ions.¹⁹ Note that such a distribution of relocation distances includes a non negligible fraction of relocation events to sites farther than nearest neighbor ones. These short-to-medium range relocations are at the origin of the stabilization of compositional patterns under irradiation.

Time evolution is followed using the residence-time algorithm,² where the frequencies of vacancy exchanges are weighted against the frequencies of random atomic relocations. The pre-exponential factor for the thermal jump is set to $10^{14}s^{-1}$, and $\Gamma(s^{-1})$ is the frequency of random atomic relocation. At each KMC step, a thermal jump or a ballistic jump is randomly chosen according to their relative probabilities, and time is incremented by the residence time of the current configuration, which is given by the inverse of the sum of frequencies for all possible events. Because of the possible trapping of vacancy on solute atoms and solute clusters, we followed the approach proposed by Soisson and coworkers,²⁶ to rescale the KMC time t_{MC} to obtain a physically meaningful time t . For alloy compositions such that the matrix phase is highly concentrated in A atoms, as in the present work, this re-scaling assumes that the physically correct vacancy concentration in a pure A phase should match the equilibrium vacancy concentration in that phase, leading to the following rescaling:

$$t = t_{MC} \frac{C_V^{MC}(A)}{C_V^{eq}(A)} \quad (3)$$

where $C_V^{MC}(A)$ is the fraction of the time spent by the vacancy when surrounded with 12 A nearest neighbors times the nominal vacancy concentration, here $1/64^3$. $C_V^{eq}(A)$ is the equilibrium vacancy concentration in pure A at the specific temperature. Such rescaling of time guarantees that the B diffusivity in the matrix remains constant during precipitation. This rescaling does not take into account radiation-enhanced diffusion (RED), for which one would need to use KMC simulations that explicitly include point defect production, migration, recombination, and elimination on sinks.²⁷ As a conse-

TABLE I. Different energetic parameters used in the study.

Parameter set	E_{coh}^A	E_{coh}^B	ϵ_{AAB}
1	-4.34 eV	-4.34 eV	0
2	-4.34 eV	-4.34 eV	± 0.005 eV
3	-4.34 eV	-4.30 eV	0
4	-4.34 eV	-4.20 eV	0

quence of the simpler KMC model used here, forcing values of γ cannot be directly compared to experimental ones. Nevertheless, the sequence of steady states predicted by the present simulations when Γ or T are varied can be directly compared to experiments.

Four parameter sets are used in this study, see Table. I. Parameter set 1 corresponds to the model and values used by Enrique and Bellon;¹⁸ in particular this set has only pairwise interactions, the same cohesive energy for A and B solids, and the same self-diffusion coefficients in pure A and pure B phases. To investigate a system with asymmetric thermodynamic properties, parameter set 2 has ϵ_{AAB} set to ± 0.005 eV, leading to asymmetric equilibrium phase diagrams, which will be discussed in Section III B. In parameter sets 3 and 4, the triplet atomic interactions are set back to zero but we introduce asymmetric diffusivities for A and B elements; this is achieved by assigning different values to the A and B cohesive energies. This kinetic asymmetry is much more pronounced in parameter set 4 than in parameter set 3, as will be detailed in Section III C. For all parameter sets, the vacancy formation energy was taken as equal for the two elements, with a value typical of pure Cu: $E_{for}^{AV} = E_{for}^{BV} = 1.28$ eV. The ordering energy $\omega = 0.0553$ eV is typical of alloy systems with moderately immiscibility, e.g., Cu-Ag. These parameters yield a positive heat of mixing of 8 kJ \cdot mol⁻¹ when triplet interactions are ignored, which results in a miscibility gap with a critical temperature $T_c = 1573$ K,^{28,29} at the equiatomic composition. The saddle point energy of the vacancy jump, E_X^{SP} is taken as a constant independent of the nature of the jumping atom X , $X = A$ or B . In this study, E_X^{SP} is set to -10.217 eV for both elements, which corresponds to a vacancy migration energy of 0.80 eV for parameter sets 1 and 2. All the simulations were carried out at the temperature of 0.036 eV. The standard simulation system used in this work contains $64 \times 64 \times 64$ sites, although some simulations were run with $128 \times 128 \times 128$ to evaluate possible finite size effects.

Simulations were run well beyond the time required to reach steady state, which was based on the evolution of internal energy and structure factor with time. Typically, up to 600 iterations of 2×10^9 jumps were employed for each run (counting both thermal and ballistic jumps), thus representing $\approx 5 \times 10^6$ jumps per atom. Furthermore, two different initial configurations were employed, namely a random solid solution and a single pure B precipitate embedded in a pure A matrix, in order to confirm

that the systems have reached steady state.

Cluster analysis is used in this study to identify and calculate the size of precipitates. A cluster is comprised of atoms that are connected by at least one first nearest neighbor bond. The number and possible clustering of matrix atoms inside a precipitate is also analyzed by the same cluster analysis algorithm.

The structure factor $S(\mathbf{k})$, defined as the Fourier transform of the pair-correlation function, is calculated to determine the characteristic length of the microstructure in the patterning regime. Since microstructures in this study are statistically isotropic, we used a spherically averaged structure factor:

$$S(k) = \frac{1}{4\pi} \int S(\mathbf{k}) d\Omega \quad (4)$$

The peak position of the $S(k)$ curve is used to identify the system's steady state regime in the dynamical phase diagram.¹⁸ When $S(k)$ is maximum for the first non-zero k point, the system is decomposed at the largest possible length scale available in that run. This is characteristic of macroscopic phase separation. In that state, the intensity of the peak of $S(k)$ scales with the simulation volume. In contrast, in the compositional patterning regime, $S(k)$ exhibits a maximum for a finite k , and the intensity of that peak is independent of the system size. Since the characteristic relocation distance R that we use here is much smaller than the system size, it is relatively easy to distinguish these two possible steady states solely based on the peak position of the structure factor. For a few ambiguous cases, we ran simulations with larger system sizes to determine the size dependence of the $S(k)$ peak and resolve the ambiguity. Lastly, the solid solution steady state is characterized by a small and size-independent $S(k)$ that decays monotonously with k .

III. RESULTS

A. Novel cherry-pit nanostructures

A - B alloys with B concentration $0.10 \leq c_B \leq 0.50$ have been studied in this work. Results shown in Sections III A, III B, III C and III D were obtained for $c_B = 0.15$ as it provides a basis to describe all steady states when only one of the two phases is connected, and thus when the matrix and precipitate phases can be unambiguously distinguished. The effect of composition is discussed in Section III E.

In this section, we first report results obtained for an $A_{85}B_{15}$ alloy using parameter set 1, that is for a system where all thermodynamic and kinetic properties are invariant under the transformation $c_A \leftrightarrow c_B$. Upon increasing Γ , while keeping other parameters constant, analysis of the structure factor shows that the system undergoes a transition from macroscopic phase separation regime to a compositional patterning regime when

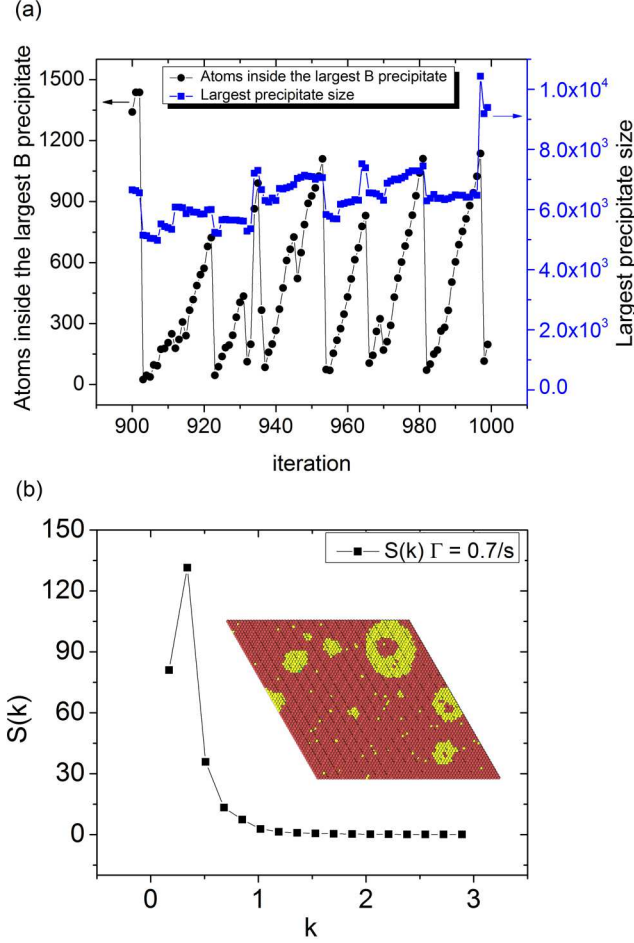


FIG. 3. (a) “Cherry” and “pit” size evolution as a function of KMC time. Data points begin from a time during steady state, and the time is set to zero. $\Gamma = 0.7 \text{ s}^{-1}$. (b) Structure factor and the microstructure shows that the system is in the patterning regime. A atoms: red, B atoms: yellow. All figures use the same color coding.

Γ exceeds 0.1 s^{-1} . This transition is in agreement with previous results reported by Enrique and Bellon¹⁷ for $c_B = 0.50$ and by Krasnochtchekov et al.⁴ for $c_B = 0.10$. The novel result however is that in the patterning regime a significant number of the precipitates, particularly larger ones, possess a sub-structure, as seen in Fig. 3(b). These precipitates are comprised of a nearly pure-A core covered by a nearly pure-B shell. In order to investigate the formation and stability of these cherry-pit structures, we employ cluster analysis, and illustrate the results of that analysis in Fig. 3(a) for $\Gamma = 0.7 \text{ s}^{-1}$.

For simplicity, we plot here only the evolution of the size of the largest B precipitate in the simulation cell, and the number of A atoms in that B precipitate, as a function of KMC iterations. As seen in Fig. 3(a), while the precipitate size remains stable, the number of A atoms inside the B precipitate evolves in a cyclic manner. We point out that, during most of a cycle, the A atom con-

centration inside the largest B precipitate greatly exceeds the equilibrium solubility limit, which is $\approx 10^{-4}$.

This large number of matrix atoms have in fact precipitated and formed the A-rich core, as seen in Fig. 3(b). A sequence of atomic configurations separated by a small number of iterations, see Fig. 4, reveals that cores first nucleate near the center of the larger B precipitates, then grow, until they make contact with the matrix phase, at which point the precipitates undergo a morphological reconstruction, leading to precipitates that are core-free. The sequence then repeats itself, unless the precipitate size changes significantly, for instance through coagulation with another precipitate, or through dissolution into the matrix. The volume fraction occupied by pits in precipitates was measured using our cluster analysis. In the present case, clusters containing 10 A atoms or more were counted as pits, but the results are not sensitive to the choice of this threshold, and a nearly identical volume fraction is obtained if we use a threshold of 30 A atoms. At steady state, for $\Gamma = 0.7 \text{ s}^{-1}$, the pit volume fraction was 4.0%. This fraction is thus small but easily detectable. Cherry-pit nanostructures persist as part of the stable steady state microstructure until Γ exceeds 15 s^{-1} , at which point the system enters the solid solution regime.

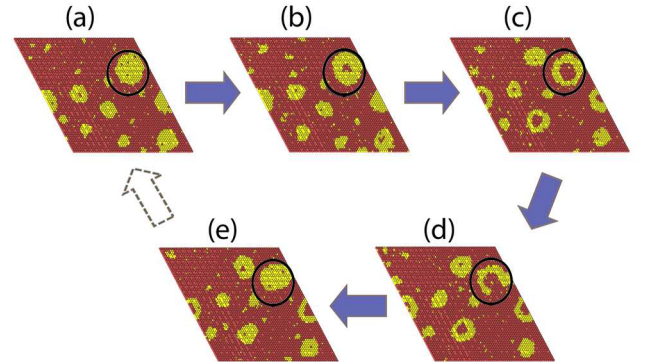


FIG. 4. Temporal evolution of the cherry-pit structure: (a) a compact B precipitate, (b) nucleation of the “pit”, (c) growth of the “pit”, (d) absorption of the “pit”, (e) recovery of a compact B precipitate. $\Gamma = 0.7 \text{ s}^{-1}$.

In summary, for the $A_{85}B_{15}$ alloy with parameter set 1, three distinct steady states are observed upon increasing Γ as previously reported by Enrique and Bellon¹⁸. In the patterning regime, however, novel cherry-pit nanostructures are observed, and patterning is not only spatial but temporal, as these cherry-pit structures undergo cyclic formation and elimination.

B. Effect of asymmetric thermodynamic interactions

In this section, we consider the effect of asymmetric thermodynamic interactions by setting the triplet atomic

interactions to $\epsilon_{AAB} = \pm 0.005$ eV, see parameter set 2 in Table I. A consequence of these asymmetric thermodynamic interactions is that the equilibrium solubilities become asymmetric. A positive (resp. negative) triplet interaction decreases (resp. increases) the equilibrium solubility of B in A , as illustrated by the low temperature part of the equilibrium phase boundaries calculated with parameter set 1 and 2, see Fig. 5. Since the temperature used in the simulations is low, $\approx 0.27T_c$, we employed a mean field approximation for this calculation, based on the mixing enthalpy given in Eq. (1). At $T = 0.036$ eV, the solubility of B atoms in A for $\epsilon_{AAB} = 0.005$ eV is about 780 times smaller than that for $\epsilon_{AAB} = -0.005$ eV, according to the mean field free energy. Note that the equilibrium solubility of A in B is obtained by exchanging A and B everywhere in Fig. 5, that is, in the x axis label, and in the subscripts of the triplet interaction parameters, using the relationship $\epsilon_{BBA} = -\epsilon_{AAB}$. A series of simulations has been carried out by increasing systematically Γ , so as to identify the sequence of steady states stabilized with parameter set 2. We identified five distinct steady states, instead of three for parameter set 1.

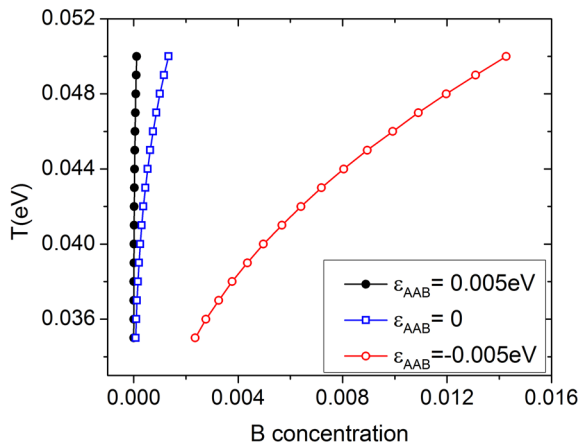


FIG. 5. Low-temperature section of the A-rich side of the equilibrium phase diagram of A - B alloy, with $\omega = 0.0553$ eV, $\epsilon_{AAB} = \pm 0.005$ eV.

For $\epsilon_{AAB} = 0.005$ eV, the steady state changes from macroscopic phase separation at $\Gamma = 0.05s^{-1}$ to compositional patterning when Γ is increased to $\Gamma = 0.1s^{-1}$. This is illustrated by the structure factors and atomic configurations shown in Fig. 6(a) and (b). Note that in both cases, the size of the largest precipitate grows as the systems approach steady state, but it exhibits discontinuities. These discontinuities result from coagulation events, which were confirmed by direct visualization of atomic configurations. More importantly, for the current discussion, the B -rich precipitates stabilized for $\Gamma = 0.1s^{-1}$ do not contain A -rich cherry pits. Furthermore, the A solubility in the largest B precipitate

remains small, $\approx 10^{-2}$. Upon increasing Γ to $0.5s^{-1}$, however, cherry-pit structures appear, see Fig. 6(c), and cluster analysis indicates that the steady-state volume fraction of the pits reaches 5.0%.

Turning now to the case where $\epsilon_{AAB} = -0.005$ eV, we observe a stabilization of cherry-pit structures before the transition from macroscopic phase separation to patterning. As illustrated in Fig. 6(d) for $\Gamma = 0.05s^{-1}$, the system is still in the macroscopically decomposed state as indicated by the high intensity of the structure factor and the presence of only one precipitate, but A -rich cores are found in this precipitate. Simulations started from configurations with one large precipitate led to a similar steady state.

In contrast to the cherry-pit structures in the compositional patterning regime, detailed visual inspection of atomic configurations reveal that several pits can simultaneously be present in one macroscopic precipitate, as illustrated in Fig. 7. As in the patterning regime, pits are absorbed by the matrix when they make contact with it. The size of the pits, however, remains small compared to the size of the macroscopic precipitate. We checked this point by comparing the pit sizes obtained for system sizes of 64^3 and 128^3 . In the latter case, the macroscopic B -rich precipitate is 8 times more voluminous, but the pit size distributions are nearly identical.

In conclusion, with asymmetric thermodynamic interactions, we identified five steady states for an $A_{85}B_{15}$ alloy: macroscopic phase separation without cherry-pit structure; macroscopic phase separation with cherry-pit; patterning regime without cherry-pit; patterning regime with cherry-pit; and disordered solid solution.

C. Effect of asymmetry in diffusion

We turn next to the effect of asymmetry of diffusion, in alloy systems with symmetric thermodynamic interactions, that is with the triplet interactions set back to zero. There are several ways to introduce a kinetic asymmetry in the present model. Following the works of Athènes et al.²⁰ and Roussel et al.²¹, we chose here to vary the relative diffusion coefficients of A and B species by changing their relative cohesive energies, while keeping all other parameters unchanged. As a result, the vacancy jumps faster when it is in a phase enriched with the species with the lower cohesive energy, here the B species. We employ separate kinetic Monte Carlo simulations to measure the thermal diffusivities of A and B monomers and small clusters for parameter sets 3 and 4, as this information plays an essential role on the formation of cherry-pit structures.

For these diffusivity measurements, a single atom or a cluster comprised of N atoms, with N ranging from ~ 80 to 800, is placed in the appropriate matrix, and the system is allowed to evolve via thermally activated vacancy jumps. The diffusivity of a cluster is measured by calculating the mean squared displacement of its cen-

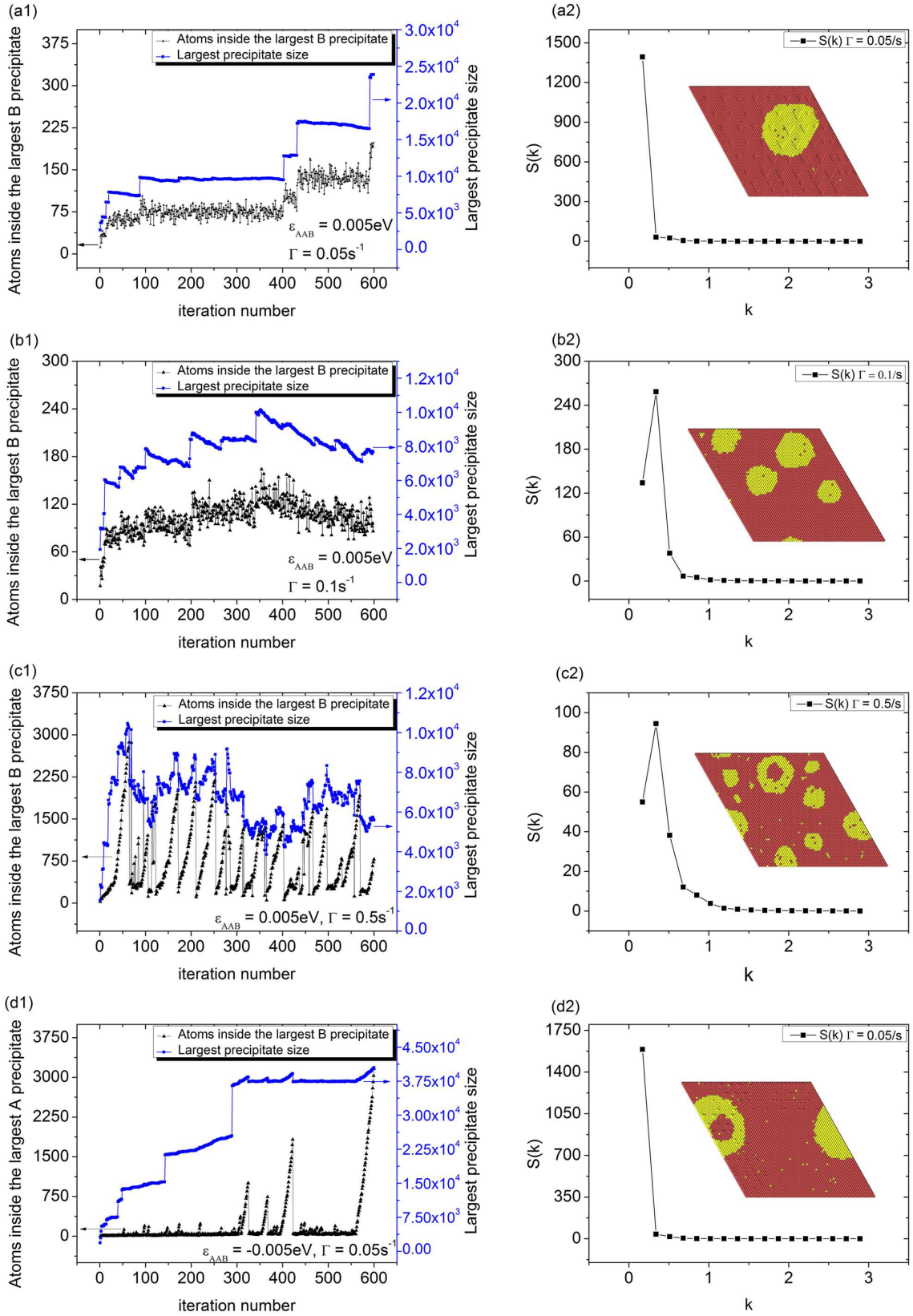


FIG. 6. Different steady states and structure factor: (a1) $\epsilon_{AAB} = 0.005 \text{ eV}$, $\Gamma = 0.05 \text{ s}^{-1}$, no cherry-pit structure (a2) macroscopic phase separation regime; (b1) $\epsilon_{AAB} = 0.005 \text{ eV}$, $\Gamma = 0.1 \text{ s}^{-1}$, no cherry-pit structure (b2) patterning regime; (c1) $\epsilon_{AAB} = 0.005 \text{ eV}$, $\Gamma = 0.5 \text{ s}^{-1}$, with cherry-pit structure (c2) patterning regime; (d1) $\epsilon_{AAB} = -0.005 \text{ eV}$, $\Gamma = 0.05 \text{ s}^{-1}$, with cherry-pit structure (d2) macroscopic phase separation regime. Atomic (111) planes of typical microstructure are shown as inset in the $S(k)$ plots.

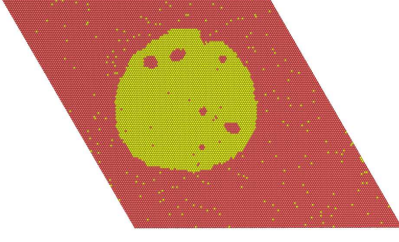


FIG. 7. Atomic plane showing the presence of multiple pits in one precipitate in the macroscopic phase separation regime. $\epsilon_{AAB} = -0.005$ eV, $\Gamma = 0.05$ s⁻¹. System size is 128×128×128.

ter of mass, according to $D = \frac{\langle R^2 \rangle}{6t}$, using a simulation box of 32×32×32. In order to account for vacancy trapping effects, time is rescaled according to Eq. (3). Note that at the temperature of interest here, 0.036 eV, the above clusters are fairly stable, losing only a few atoms during the early stage of the simulations. Afterwards, the cluster remains stable, and the average cluster size can be calculated. For parameter set 3, as expected, the diffusion coefficients of *A* single atoms and *A* clusters migrating in a pure *B* matrix are larger than those for the migration of *B* atoms and clusters in an *A* matrix. For single atom diffusion, we can directly compare our KMC data with the standard five-frequency model³⁰, and as expected, the agreement is excellent, see Fig. 8(a). With parameter set 3, the *A* impurity diffusion coefficient is ≈ 20 times faster than that of the *B* impurity. Furthermore, small *A* clusters migrate also faster than their *B* counterpart. Since the diffusivity of *A* clusters decreases significantly with cluster size, one can anticipate that if a pit forms, it will act as a trap for individual *A* atoms and small *A* atom clusters, thus stabilizing the pit.

Similar cluster diffusivity results were obtained for parameter set 4, but with a larger difference between the diffusivities of *A* and *B* species since the difference in cohesive energies between the pure metals is much larger than for parameter set 3. The diffusion coefficient of *A* monomers, for instance, is five orders of magnitude faster than that of *B* monomers, as seen in Fig. 8(b).

We return now to our study of steady states stabilized by irradiation, starting with parameter set 3. Upon increasing Γ , the steady state changes from macroscopic phase separation, for $\Gamma = 0.1$ s⁻¹, to compositional patterning for $\Gamma = 0.5$ s⁻¹. For this moderately low Γ value, no cherry-pit structures are found in the compositional patterning regime, as illustrated in Fig. 9 (a1) and (a2). At larger Γ values, however, cherry-pit structures are stabilized, as shown in Fig. 9 (b1) and (b2) for $\Gamma = 2.0$ s⁻¹. At much larger Γ values, the system is driven into a disordered solid solution. This sequence of steady states is therefore qualitatively identical to the ones observed for parameter set 2 with $\epsilon_{AAB} = 0.005$ eV.

In the case of high kinetic asymmetry, that is with parameter set 4, a different sequence of steady states

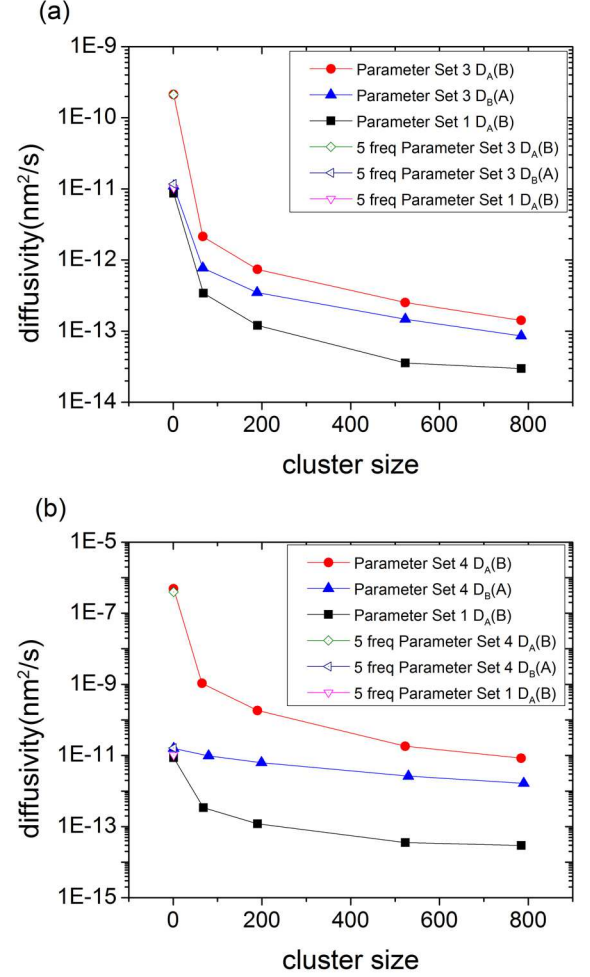


FIG. 8. Diffusion coefficients of clusters of *N* *A* atoms measured by Kinetic Monte Carlo simulations at 0.036 eV. (a) parameter set 3; (b) parameter set 4. Monomer diffusivities calculated by five-frequency model are also included.

is observed. Namely, cherry-pit structures are never found, and the system simply undergoes transition from macroscopic phase separation to compositional patterning without cherry-pit to solid solution as Γ is increased. In the compositional patterning regime, the *A* concentration in the largest *B* precipitate remains always small, never exceeding ≈ 0.01 . Direct visualization of atomic configurations supports the idea that *A* pits could not form because of the very high mobility of the *A* atoms in the precipitate compared to the rate of ballistic mixing.

D. Effect of ballistic jump relocation distance

All the simulation results reported in the previous sections were carried out using a ballistic jump relocation distance of $R = 1.08a_{nn}$, a value chosen based on MD simulations modeling the ballistic mixing produced by 1MeV Kr irradiation in equiatomic Cu-Ag alloy¹⁹. It is

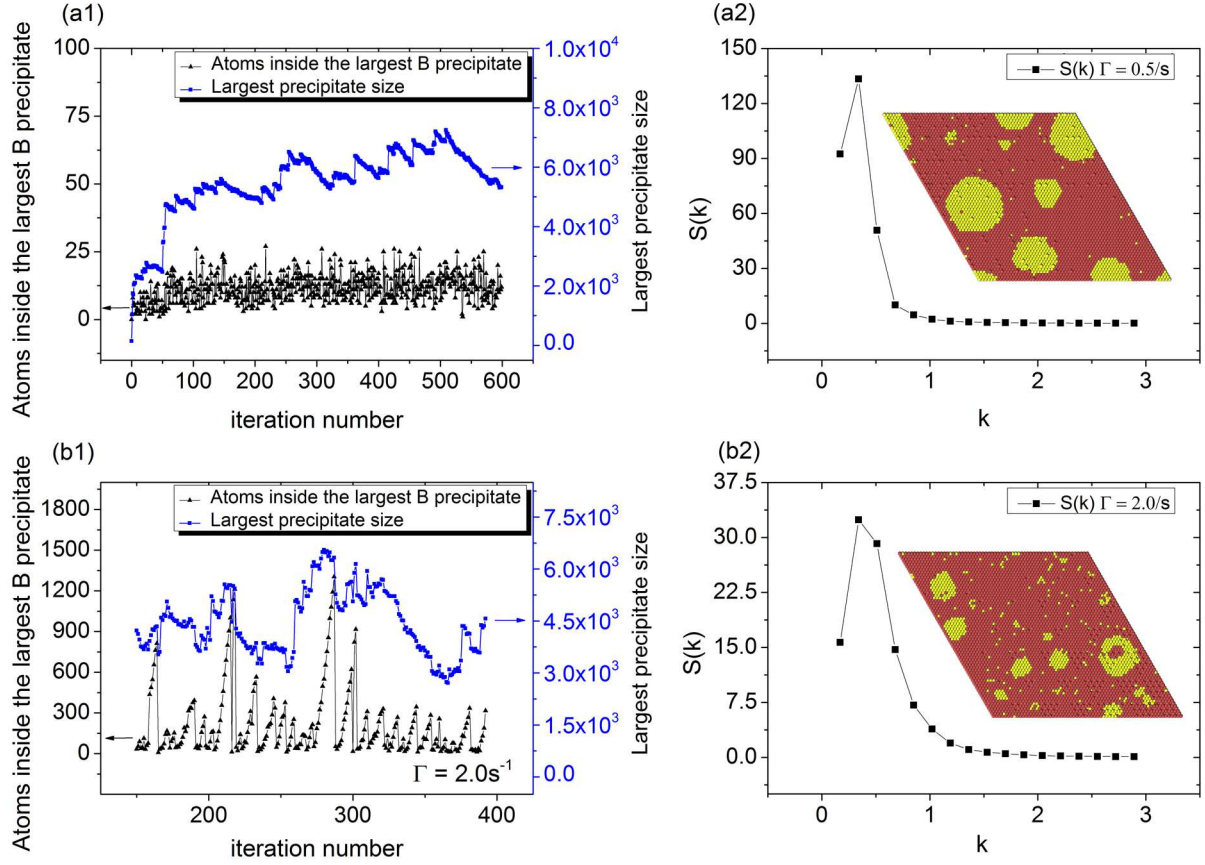


FIG. 9. Cluster analysis result for simulation with $E_{BB} = -4.30 \text{ eV}$. (a1) $\Gamma = 0.5 \text{ s}^{-1}$, no cherry-pit structures (a2) Patterning regime (a1) $\Gamma = 2.0 \text{ s}^{-1}$, with cherry-pit structures (a2) Patterning regime. Atomic (111) planes of typical microstructure are inserted in the $S(k)$ plots.

nevertheless useful to investigate the effect of the relocation distance on the stability of cherry-pit structures. For instance, for parameter set 2 with $R = 1.08a_{nn}$ and $\Gamma = 0.1 \text{ s}^{-1}$ cherry-pit structure is not observed. However, if the value of R is increased to $2.16a_{nn}$ and $3.24a_{nn}$, as shown in Fig. 10, cherry-pit structures form. Simulations were used to determine the boundary in the (R, Γ) plane between the regimes where cherry-pit structures were present and absent, for parameter sets 1 and 2, as summarized in Fig. 10. This boundary is well approximated by the equation $\Gamma R^n = C_{CP}$ with $n \approx 3.5$, and with C_{CP} a constant. The functional dependence of the stability boundary for cherry-pit structures as well as the value of C_{CP} will be discussed in Section IV.

E. Effect of concentration

In previous sections, the KMC simulations were performed for an average B -concentration of 15%. This concentration facilitated the identification of the cherry-pit structures as it provided a large volume fraction of isolated B -rich precipitates. As the B concentration is increased, the precipitate phase percolates, and

one is left with a bi-connected two-phase microstructure, as reported by Enrique and Bellon for equiatomic compositions.^{18,19} We present here some results obtained for 25% and 40% B concentration, to illustrate this evolution of the microstructure in the patterning regime. In the case of $c_B = 25\%$, the B rich precipitate phase has percolated, as seen in Fig. 11(a). This is not surprising since the static percolation threshold for fcc lattices is $\approx 20\%$;³¹ more importantly the microstructure under irradiation undergoes kinetic roughening under the above conditions,³² leading to non-compact precipitate shapes. While cherry-pit structures can also be identified once the B -rich phase has percolated, the transition from macroscopic phase-separation to compositional patterning is difficult to identify since the presence of one large B -rich phase spanning the whole simulation system in the patterning regime leads to a structure factor that is very similar to the one characteristic of macroscopic phase separation. In particular, these structure factors present a peak for the smallest non-zero k vector, and the intensity of this peak scales linearly with the simulation volume. Percolation and double connectivity of the microstructure become even more evident for simulations performed for $c_B = 40\%$, as seen in Fig.

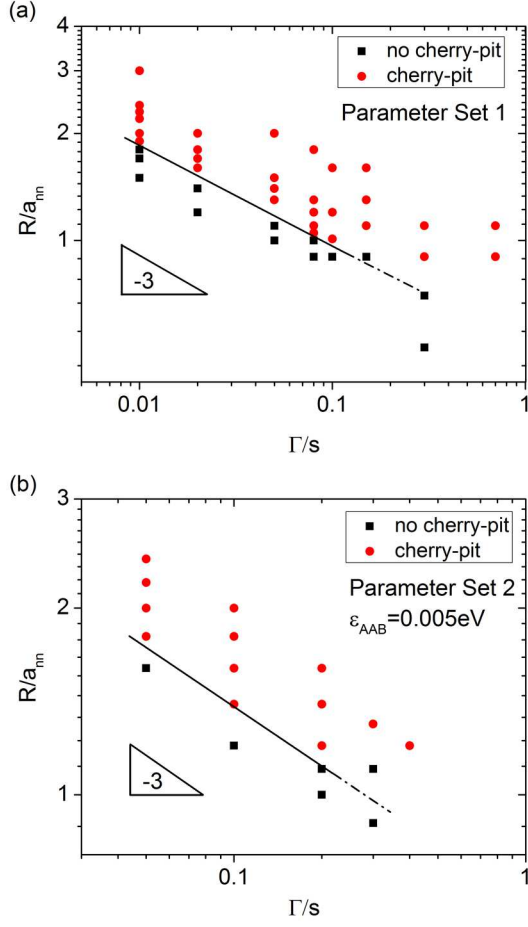


FIG. 10. Cherry-pit structure formation affected by different relocation distance. Power law fitting of the cherry-pit structure formation boundaries are provided in both plots. (a) parameter set 1; (b) parameter set 2.

11(b). Notice that in this case, the cherry-pit structure has evolved into a three dimensional bi-connected structure, with a finite characteristic length scale. As a result, the corresponding structure factor does display a maximum for a finite k vector, with an intensity that is independent of the system size, thus making it easy again to distinguish macroscopic phase separation from compositional patterning. In summary, the dynamical stabilization of cherry-pit structures is best observed for compositions ranging from $c_B \approx 10\%$ to 20% . These composition boundaries may of course vary with irradiation conditions and with thermodynamic and kinetic parameters of the alloy of interest.

IV. DISCUSSION

The central result presented here is the dynamical stabilization of novel non-equilibrium precipitate structures in alloys subjected to energetic ion irradiation. These

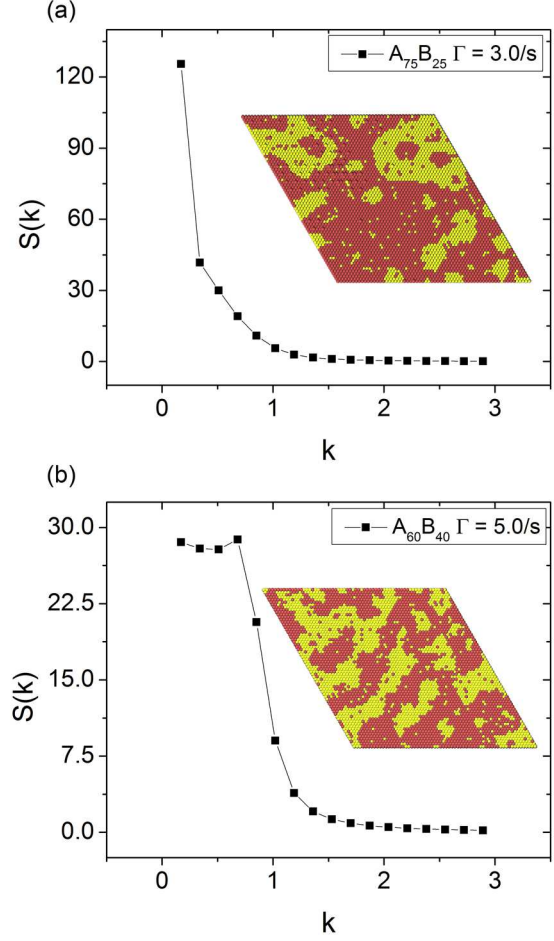


FIG. 11. Effect of different concentrations on cherry-pit structures. (a) $A_{75}B_{25}$, $\Gamma = 3.0s^{-1}$, (b) $A_{60}B_{40}$, $\Gamma = 5.0s^{-1}$.

novel structures, which we referred to as cherry-pit structures, are observed in KMC simulations of $A_{1-c}B_c$ binary model alloy systems where ballistic mixing competes with thermally-activated decomposition. These structures are observed near the dynamical transition between the steady states of macroscopic phase separation and compositional patterning. In the compositional patterning regime, the maximum pit size is bounded by the steady-state precipitate size, which maximum size is about $2\pi R$,^{17,18} where R is the characteristic length scale of the ballistic atomic relocations. Interestingly, a similar size limitation is also measured for pit structures forming in macroscopic B -rich precipitates. In addition, simulations reveal that these cherry-pit structures display temporal organization, and that the pits go through repeated cycles of nucleation, growth, and absorption by the matrix, as illustrated in Fig. 3 and Fig. 4. Analysis of these dynamical cycles suggests that they are nearly periodic, although a significant scattering is observed from cycle to cycle within one precipitate, and from precipitate to precipitate. This scattering results from the dis-

person introduced by variable incubation times for pit nucleation, and from the dispersion of precipitate sizes under steady-state conditions.

In order to investigate the processes controlling the kinetics of pit dynamics, we measured the average pit life-time as a function of precipitate size. It was found that the pit life-time increased nearly linearly with the precipitate size. A related characteristic of the kinetic evolution of pits is that, after their nucleation, their volume tends to grow nearly linearly in time. Since precipitate sizes are largely constant at the short time scale relevant for pit nucleation, growth and absorption, a linear growth kinetics is consistent with a linear dependence of the pit life-time with precipitate size. These dependencies can be understood by assuming that pits, once nucleated, grow by trapping the A atoms ballistically recoiled from the matrix into the precipitates.

We have shown in Sections III B, III C and III D that the conditions required for the stabilization of cherry-pit structures are strongly dependent on thermodynamic and kinetic parameters of the alloy system, as well as of the relocation range R . We propose here to rationalize these effects by extending the model introduced by Frost and Russell^{13,14} for irradiation-induced compositional patterning. In that model, one considers pure B precipitates of fixed radius r_p to calculate the solute concentration profile in the matrix in the presence of ballistic relocations of length R . One then solves a diffusion equation for the solute atoms, here the B atoms, assuming that their transport between precipitates is purely controlled by thermally activated diffusion. The ballistic mixing is reduced to a source term, resulting from the injection of B atoms from the precipitate into the matrix. This source term is a function of r , the distance to the center of the precipitate:

$$G(r) = \frac{\Gamma}{4Rr} [r_p^2 - (r - R)^2] \quad (r > r_p) \quad (5)$$

The steady-state solution of this diffusion equation yields the following expression for the steady-state solubility of B atoms in the matrix forced by ballistic mixing:

$$c_B^{bal} = \frac{\Gamma R^2}{12D_B} \left(1 - \frac{R}{4r_p}\right) \quad (6)$$

where D_B is the impurity diffusion coefficient of B atoms in a pure A matrix. As the above model does not include thermal solubility or capillary (Gibbs-Thomson) effects, Frost and Russell proposed to superimpose to the previous solubility the standard thermal contribution expected for a precipitate-matrix system. The resulting total solubility limit under irradiation then writes

$$c_B^{irr} = c_B^{eq,\infty} \left(1 + \frac{2\sigma V_B}{r_p k_B T}\right) + \frac{\Gamma R^2}{12D_B} \left(1 - \frac{R}{4r_p}\right) \quad (7)$$

where $c_B^{eq,\infty}$ is the B equilibrium solubility for a planar interface, σ is the interfacial energy and V_B the atomic volume in the precipitate, which is assumed to be pure B . As noted by Frost and Russell, two terms contribute to the dependence of the solubility with the precipitate radius, one due to the Gibbs-Thomson effect, and one from ballistic mixing. Since these two terms have identical functional dependence, both scaling as $1/r_p$, they can be grouped together, and recast into an effective Gibbs-Thomson equation, with an effective capillary length. As the ballistic frequency Γ increases, the effective capillary length is reduced, and eventually becomes negative. Frost and Russell proposed to identify the Γ value at which the capillary length becomes negative as the boundary between equilibrium-like phase separation and patterning. A similar but more detailed analysis of this inverse coarsening can be found in the work of Heinig et al.³³ This critical value for the transition between these two steady states, Γ_{MPS-CP} takes the following expression

$$\Gamma_{MPS-CP} = c_B^{eq,\infty} D_B \left(\frac{96\sigma V_B}{k_B T}\right) \frac{1}{R^3} \quad (8)$$

We note that this model predicts that, in the (R, Γ) parameter space, the boundary between the two steady states is given a condition $R^3 \times \Gamma = \text{constant}$. This functional dependence of the boundary with R and Γ is in agreement with the analytical model of Enrique and Bellon in the so-called “strong-segregation” regime,^{17,18} that is far from the critical point (R_c, γ_c) in Fig. 2. In the context of the present simulations, two important conclusions from the above equation are that the critical ballistic frequency for the transition from macroscopic phase separation to compositional patterning scales linearly with the B equilibrium solubility and with the B impurity diffusion coefficient.

We propose now to extend Frost and Russell’s model to atomic diffusion *inside* a precipitate.³⁴ We need to consider the flux of A atoms that are ballistically recoiled from the matrix into the precipitate, which are again assumed to be pure B . From simple geometric considerations, we derive the corresponding source term

$$G(r) = \frac{\Gamma}{4Rr} [(R + r)^2 - r_p^2] \quad (r < r_p) \quad (9)$$

Following the approach employed by Frost and Russell, we calculate an expression for the steady-state solubility of A in the precipitate, and add the expected Gibbs-Thomson contribution, yielding the following expression for the total A solubility

$$c_A^{irr} = c_A^{eq,\infty} \left(1 - \frac{2\sigma V_A}{r_p k_B T}\right) + \frac{\Gamma R^2}{12D_A} \left(1 + \frac{R}{4r_p}\right) \quad (10)$$

Notice that this time, the signs of the two terms contributing to capillary effects are opposite to the ones

found when solving for B solubility in the matrix phase, see Eq. (7). Again, one can define an effective capillary length. As the ballistic frequency Γ increases, this effective capillary length decreases, then goes to zero, and becomes negative. We propose that a negative capillary length inside the precipitate corresponds to the onset of precipitation of A atoms inside the B precipitate, and it corresponds to the formation of a cherry-pit structure. The critical ballistic frequency for the transition from no cherry-pit to cherry-pits is given by

$$\Gamma_{CP} = c_A^{eq,\infty} D_A \left(\frac{96\sigma V_A}{k_B T} \right) \frac{1}{R^3} \quad (11)$$

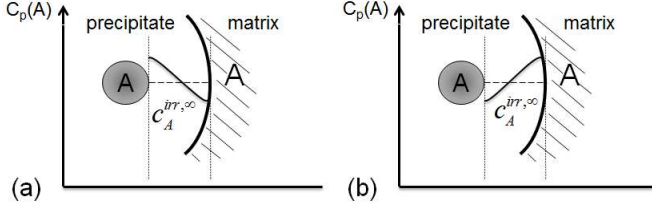


FIG. 12. Schematic A concentration profiles in a B -rich precipitate, $C_p(A)$, between an A -rich pit, in grey, and the precipitate-matrix interface. The steady-state concentration in local equilibrium with a flat interface under irradiation, $c_A^{irr,\infty}$, is shown as a horizontal dashed line. (a) positive effective capillary length; (b) negative effective capillary length.

The origin of the stabilization of the A -rich pits can be understood by considering the A compositions in local equilibrium with the relevant interfaces, as depicted in Fig. 12. When the effective capillary length, deduced from Eq. (11), is positive, the local A solubility in a B -rich precipitate is larger at the pit-precipitate interface than it is at the precipitate-matrix interface, as illustrated in Fig. 12(a). It is therefore expected that A atoms will flow from the pit to the matrix, and thus that pits are not stable. Note that this is also the case for systems at thermodynamic equilibrium. In contrast, when irradiation conditions are such that this effective capillary length is negative, as in Fig. 12(b), the situation is reversed, and A atoms should now flow from the precipitate-matrix interface to the pit-precipitate interface, leading to the continuous growth of the pit, as observed in the KMC simulations.

Returning to the model, one first notes the similarity between Eq. (11) and the one derived by Frost and Russell for the onset of patterning, Eq. (8). In particular, the functional dependence of the boundary with respect to R and Γ is again given by $R^3 \times \Gamma = \text{constant} = C_{CP}$. We tested this functional dependence using the KMC simulation results presented in Fig. 10 for parameter sets 1 and 2. As seen from the figure, the agreement is quite good, with the best fit to the data giving a boundary for $R^n \times \Gamma = \text{constant}$ with $n = 3.52$ for parameter set 1 and

$n = 3.46$ for parameter set 2. We note that these values are between the values identified by Enrique et al.¹⁷ of $n = 3$ for the strong segregation regime (i.e., far from γ_c) and $n = 4$ for the weak segregation regime (i.e., close to γ_c). Another important result from Eq. (11) is that the critical ballistic jump frequency for the stabilization of cherry-pits scales linearly with the A equilibrium solubility and with the A impurity diffusion coefficient. Note that in the Frost and Russell model, and in its extension proposed here, all ballistic events have the exact same relocation distance. Heinig et al.³³ showed however that an exponential distribution of relocation distances leads to results identical to Eqs. (6, 7, 8), except for different numerical coefficients. These differences do not affect the functional dependences of the transition from macroscopic phase separation to compositional patterning, and those of the stability boundary of the cherry-pit regime. It is therefore meaningful to compare these analytical functional dependences with our KMC data.

We can now compare the steady states identified in the KMC simulations with those predicted by this extended patterning model. First, in the case of a fully symmetric alloy system, as for parameter set 1, the equilibrium solubilities and the impurity diffusion coefficients are identical for A and B atoms. We thus expect that, as Γ is increased, the onset of compositional patterning (the boundary labeled γ_1 in Fig. 2) coincides with the onset of the formation of cherry-pit structures. This is indeed what was found for parameter set 1, see Section III A. We turn then to the case of alloy systems that have asymmetric solubilities but symmetric diffusion properties, parameter set 2. When the B equilibrium solubility in A is lower than that of A in B , that is for positive values of ϵ_{AAB} , the extended patterning model predicts that, as Γ is increased, the system will first undergo a transition from macroscopic phase separation to compositional patterning before entering the domain of cherry-pit formation. This is also in agreement with the KMC results summarized in Fig. 6(a-c). Conversely, when the B equilibrium solubility is larger than that of the A solubility, that is for negative values of ϵ_{AAB} , the extended patterning model predicts that cherry-pit structures will become stable while the system is still in the macroscopic phase separation steady state, again in qualitative agreement with our simulation results, see Fig. 6(d). In both cases, however, the quantitative agreement with the model is limited in the sense that the model predicts that for positive ϵ_{AAB} values the domain over which compositional patterning would be stabilized without cherry-pit structures should cover three decades in Γ according to Eqs. (8), (11), in contrast to the one decade found in the KMC simulations. We believe that this overestimation is due to the approximations made in the model, in particular the assumption that the matrix and precipitate phases are pure A and pure B phases, respectively, and the fact that the ballistic and thermal solubilities are derived separately.

We turn now to the case of alloy systems that have

symmetric thermodynamic interactions but asymmetric impurity diffusion coefficients, as in parameter sets 3 and 4. In this case again, the sequence of steady states predicted by the extended patterning model is in agreement with the simulation results reported in Section III C. For instance, an increase of A atom diffusivity over that of B atoms is expected to shift the onset of cherry-pit formation to larger Γ values than those required for compositional patterning. In this case, the agreement between the KMC simulations and the model is even semi-quantitative, as the ratio of Γ values for the transition from macroscopic phase separation to compositional patterning, $\Gamma \approx 0.1s^{-1}$, to the transition for no cherry-pit to cherry-pit, $\Gamma \approx 2.0s^{-1}$, is in the ratio of $D_B(A)$ over $D_A(B)$, as expected from Eqs. (8), (11). For parameter set 4, this shift is expected to be very large since the A and B diffusivities differ by 5 orders of magnitude. The fact that no cherry-pit structures are observed for parameter set 4 can then simply be understood as a case where the very large diffusional asymmetry shifted the possible cherry-pit formation to Γ values larger than the boundary between the compositional patterning and solid solution steady states, the boundary labeled γ_2 in Fig. 2.

The stabilization of cherry-pit structures is reminiscent of the transient formation of small clusters around a precipitate undergoing dissolution, under irradiation.^{33,35} Cherry-pit structures are also reminiscent of the stabilization of similar inverted structures in equilibrium systems with competing interactions. Indeed, following approaches introduced by Martin³⁶, Vaks and coworkers³⁷ and Garrido and coworkers³⁸, Enrique and Bellon³⁹ showed that the dynamical steady states reached under irradiation can be described as thermodynamic equilibrium states in systems with effective interactions. Specifically, for the alloy systems considered here, the effective interactions between like atoms would be comprised of short-range attractive interactions, due to the thermodynamics of the systems, and long range repulsive interactions, resulting from the finite-range ballistic mixing. Such a competition can be found in physical systems, for instance in the two-phase phospholipid systems studied by McConnell and coworkers.^{40–42} In these thin film systems, a solid-liquid phase co-existence results from a competition between short-range attractive chemical interactions with long-range repulsive dipolar interactions. As shown analytically,⁴² and observed experimentally^{40,43}, this competition generates morphological instabilities of lipid domains, and in particular, above a critical size, spherical domains undergo a first-order transition from a disc to a torus, which is the two-dimensional equivalent of the transition from compact sphere to cherry-pit structures in three-dimensions.

One remarkable characteristics of the cherry-pit structures reported here is their near periodic cyclic evolution. This can be rationalized by considering the three characteristic time scales relevant for these evolutions, namely the pit nucleation time, the pit growth time, and the precipitate life time. For the parameters employed in

this study, KMC simulations reveal that the three time scales are well separated. As a consequence, in the pit formation regime, starting from a pristine precipitate, a pit nucleates quickly, then grows relatively slowly, and is finally absorbed by the matrix when it intercepts the precipitate-matrix interface, which has barely changed over this one cycle. Furthermore, for a given precipitate size, the pit growth rate is nearly identical from one cycle to the next, since this growth rate is controlled by the recoil of A atoms from the matrix into the precipitate. As a consequence, the pit evolution cycles are nearly periodic.

Finally, we point out that in recent experiments on $\text{Cu}_{1-x}\text{Fe}_x$ and $\text{Cu}_{1-x}\text{V}_x$ (with $x \approx 10 \text{ at\%}$) thin films subjected to 1.8 MeV Kr ion irradiation, Stumphy et al.⁸ observed by atom probe tomography inner precipitate structures similar to the cherry-pit structures reported here from KMC simulations, as illustrated by comparing Fig. 1 with Fig. 7. Interestingly, these inner precipitate structures are observed in Cu-Fe in the macroscopic phase separation regime as well as in the compositional patterning regime, where as in Cu-V they are only observed in the patterning regime. Our present study indicates that thermodynamic and kinetic asymmetries can be responsible for these differences. It is not yet known whether the nanostructures observed experimentally are dynamical, cyclic structures, as the ones revealed by the KMC simulations. A detailed comparison between experimental results and the present simulations and modeling will be offered elsewhere.⁴⁴

V. CONCLUSION

We investigate by kinetic Monte Carlo simulations in binary A-B alloys the possible stabilization by irradiation of precipitate-within-precipitate structures, which we refer to as cherry-pit structures. The simulations indicate that these structures should be stable for a broad range of thermodynamic and kinetic parameters, and that the asymmetry of these parameters influence greatly the domain of stability of the cherry-pit structures. Moreover, in the simulations, these structures display a dynamical, near-periodic, behavior, going through cycles of pit nucleation, growth, and absorption by the matrix/precipitate interface. An analytical model is proposed by extending the model previously introduced by Frost and Russell^{13,14} to include the dynamics of pit formation and stability inside precipitates. The effect of thermodynamic and kinetic alloy asymmetry on cherry-pit stabilization is in very good qualitative agreement with the KMC simulations. The simulations also offer a framework to rationalize the formation of nanostructures within precipitates recently reported by atom probe tomography in ion-irradiated Cu-Fe and Cu-V alloys.

ACKNOWLEDGMENTS

This research was supported by NSF under Grant DMR 08-04615. The authors thank Dr. Georges Martin and Xuan Zhang for stimulating discussions.

-
- ¹ G. Nicolis and I. Prigogine, *Self-organization in nonequilibrium systems: from dissipative structures to order through fluctuations* (Wiley, 1977).
 - ² G. Martin and P. Bellon, *Solid State Phys.* **50**, 189 (1997).
 - ³ R. Nelson, J. Hudson, and D. Mazey, *J. Nucl. Mater.* **44**, 318 (1972).
 - ⁴ P. Krasnochtchekov, R. S. Averback, and P. Bellon, *Phys. Rev. B* **72**, 174102 (2001).
 - ⁵ S. Chee, B. Stumphy, N. Vo, R. S. Averback, and P. Bellon, *Acta Mater.* **58**, 4088 (2010).
 - ⁶ G. Rizza, M. Strobel, K. Heinig, and H. Bernas, *Nuclear Instruments and Methods in Physics Research, Section B: Beam Interactions with Materials and Atoms* **178**, 78 (2001).
 - ⁷ G. Rizza, H. Cheverry, T. Gacoin, A. Lamasson, and S. Henry, *Journal of Applied Physics* **101** (2007).
 - ⁸ B. Stumphy, S. W. Chee, N. Q. Vo, R. S. Averback, P. Bellon, and M. Ghafari, "to be submitted," (2013).
 - ⁹ C. B. Fuller, J. L. Murray, and D. N. Seidman, *Acta Materialia* **53**, 5401 (2005).
 - ¹⁰ K. E. Knipling, R. A. Karnesky, C. P. Lee, D. C. Dunand, and D. N. Seidman, *Acta Materialia* **58**, 5184 (2010).
 - ¹¹ E. Clouet, L. Lae, T. Epicier, W. Lefebvre, M. Nastar, and A. Deschamps, *Nature Materials* **5**, 482 (2006).
 - ¹² J. A. Hanson, C. B. Chang, S. M. Graves, Z. Li, T. G. Mason, and T. J. Deming, *Nature* **455**, 85 (2008).
 - ¹³ H. Frost and K. Russell, *J. Nucl. Mater.* **104**, 1427 (1981).
 - ¹⁴ H. Frost and K. Russell, *Acta Metallurgica* **30**, 953 (1982).
 - ¹⁵ P. Bellon, in *MATERIALS SCIENCE WITH ION BEAMS*, Topics in Applied Physics, Vol. 116, edited by Bernas, H (2010) pp. 29–52.
 - ¹⁶ R. S. Averback and T. de la Rubia, *Solid State Physics - Advances in Research and Applications* **51**, 281 (1997).
 - ¹⁷ R. A. Enrique and P. Bellon, *Phys. Rev. Lett.* **84**, 2885 (2000).
 - ¹⁸ R. A. Enrique and P. Bellon, *Phys. Rev. B* **63**, 134111 (2001).
 - ¹⁹ R. A. Enrique, K. Nordlund, R. S. Averback, and P. Bellon, *J. Appl. Phys.* **93**, 2917 (2003).
 - ²⁰ M. Athènes, P. Bellon, and G. Martin, *Acta Mater.* **48**, 2675 (2000).
 - ²¹ J.-M. Roussel and P. Bellon, *Phys. Rev. B* **63**, 184114 (2001).
 - ²² J.-M. Roussel and P. Bellon, *Phys. Rev. B* **73**, 085403 (2006).
 - ²³ P. Krasnochtchekov, R. S. Averback, and P. Bellon, *Phys. Rev. B* **75**, 144107 (2007).
 - ²⁴ M. Doyama and J. Koehler, *Acta Metallurgica* **24**, 871 (1976).
 - ²⁵ N. Saunders and A. P. Miodownik, *CALPHAD: A Comprehensive Guide* (Oxford, New York, 1998).
 - ²⁶ F. Soisson and C. C. Fu, *Phys. Rev. B* **76**, 214102 (2007).
 - ²⁷ F. Soisson, *Phil. Mag.* **85**, 489 (2005).
 - ²⁸ R. Kutner, K. Binder, and K. W. Kehr, *Phys. Rev. B* **26**, 2967 (1982).
 - ²⁹ R. A. Enrique and P. Bellon, *Phys. Rev. B* **60**, 14649 (1999).
 - ³⁰ A. L. Claire, *J. Nucl. Mater.* **69-70**, 70 (1978).
 - ³¹ C. Lorenz and R. Ziff, *Journal of Physics A: Mathematical and General* **31**, 8147 (1998).
 - ³² P. Bellon, *Phys. Rev. Lett.* **81**, 4176 (1998).
 - ³³ K. Heinig, T. Müller, B. Schmidt, M. Strobel, and W. Möller, *Appl. Phys. A* **77**, 1725 (2003).
 - ³⁴ Although the more complete theory of Enrique and Bellon should be applied, this geometry of precipitates within a sphere does not lend itself to an analytical solution.
 - ³⁵ K. Russell, *J. Nucl. Mater.* **206**, 129 (1993).
 - ³⁶ G. Martin, *Phys. Rev. B* **30**, 1424 (1984).
 - ³⁷ V. Vaks and V. Kamysenko, *Phys. Lett. A* **177**, 269 (1993).
 - ³⁸ P. L. Garrido and J. Marro, *Phys. Rev. Lett.* **62**, 1929 (1989).
 - ³⁹ R. A. Enrique and P. Bellon, *Phys. Rev. B* **70**, 224106 (2004).
 - ⁴⁰ R. Weis and H. McConnell, *J. Phys. Chem.* **89**, 4453 (1985).
 - ⁴¹ D. Keller, J. Korb, and H. McConnell, *J. Phys. Chem.* **91**, 6417 (1987).
 - ⁴² H. McConnell and V. Moy, *J. Phys. Chem.* **92**, 4520 (1988).
 - ⁴³ H. McConnell, *Annu. Rev. Phys. Chem.* **42**, 171 (1991).
 - ⁴⁴ B. Stumphy, R. S. Averback, and P. Bellon, "in preparation," (2013).